

# Influence of Electrolyte on the Electrochemical Performance of the Biomass-Derived Hard Carbon for Potassium Ion Batteries

Raghunath Sahoo,<sup>[a, b]</sup> Subramanian Venkatachalam,<sup>[b]</sup> and Ramaprabhu Sundara<sup>\*[a]</sup>

There is a promising aspect of potassium-ion batteries (KIB) alternative to lithium-ion batteries (LIB) due to a similar charge storage mechanism. However, the major hurdles, such as higher volume pulverization during continuous cycling, lower Coulombic efficiency, and subsequent fading, need to be addressed before the commercialization of KIB. In this regard, the choice of electrolytes and their impact on the electrochemical performance of the electrode is quite crucial. Here, a two-step pyrolysis method was used to synthesize hard coconut shell-derived hard carbon (HHC). The synthesized powder was characterized by various analytical techniques to confirm the formation of pyrolyzed carbon. The surface area of the synthesized powder was calculated to be around  $40.9 \text{ m}^2 \cdot \text{g}^{-1}$ . Three types of electrolytes such as 1 M  $\text{KPF}_6$  in EC: DEC (1:1 v/v), 0.8 M  $\text{KPF}_6$  in EC: DEC (1:1 v/v), and 1 M KTFSI in TEGDME, were prepared to

study the electrochemical performance of the assembled KIB cell. The study demonstrated that compared to other electrolytes, 0.8 M  $\text{KPF}_6$  in EC: DEC (1:1 v/v) exhibited higher coulombic efficiency, higher charge storage capacity, and much better capacity retention. The EIS studies revealed that a lower solution resistance and a higher pseudo capacitance have aided in better electrochemical performance for 0.8 M  $\text{KPF}_6$  in EC: DEC (1:1 v/v) electrolyte. The cell exhibited a higher specific capacity of  $187.3 \text{ mAh g}^{-1}$  at a current density of  $200 \text{ mA g}^{-1}$  with a higher coulombic efficiency of 96.8% and retained about 86.7% of the original capacity after 100 cycles of charge-discharge. This promising combination of appropriate electrolytes and electrodes can further advance the research progress of potassium ion batteries.

## Introduction

The demand for electric vehicles (EVs) over traditional fossil fuel-operated vehicles is on the rise owing to the enhanced carbon footprints in the environment.<sup>[1,2]</sup> The Indian government has set a primary target to achieve 30% of new car sales to be electric.<sup>[3]</sup> The share of the expenditure on batteries in large-scale electric vehicles is set to be reduced from 49% (2016) to 19% (2030).<sup>[4]</sup> These can be achieved by the development of other battery types than commercially established LIBs. KIBs are a part of the post-LIBs, which have attracted researchers due to similar storage mechanisms like Li (rocking chair). Along with this, K has a better reduction potential ( $-2.93 \text{ V}$  vs. SHE) than Na ( $-2.71 \text{ V}$  vs. SHE) and is comparable to Li ( $-3.04 \text{ V}$  vs. SHE), which can lead to a higher potential window. In fact,  $\text{K}^+$  has the lowest Stoke's radius in organic solvents like polycarbonate (PC) than  $\text{Li}^+$  and  $\text{Na}^+$ . These lucrative advantages are overshadowed by some of the disadvantages of  $\text{K}^+$ , such as a higher ionic radius of  $0.133 \text{ nm}$  compared to  $0.95 \text{ nm}$  of  $\text{Na}^+$  and  $0.60 \text{ nm}$  of  $\text{Li}^+$ . During the frequent charging and discharging, the higher ionic radii of K ions disturb the internal structure of the electrode materials,

resulting in lower specific capacity, lower Coulombic efficiency, and poor rate capability.<sup>[5–7]</sup> Therefore, the choice of electrode and electrolyte materials needs careful consideration.<sup>[8–11]</sup>

Carbon materials are highly preferred as anode materials due to their low cost, abundance, good electrical conductivity, and good stability.<sup>[12,13]</sup> Like in the case of LIBs, graphite has been used as an anode material for KIBs, delivering a similar specific capacity of  $273 \text{ mAh g}^{-1}$ .<sup>[14]</sup> However, enormous volume changes of 61% after repeated cycling make way for an alternative anode material. K ions require a larger interplanar spacing for smoother intercalation due to a higher ionic radius. Hard carbon (HC), with a larger interplanar spacing than graphite interplanar spacing ( $0.34 \text{ nm}$ ), has recently gained much interest in the choice of anode materials.<sup>[15,16]</sup> In this regard, biomass-derived hard carbon has been studied due to its availability, low cost, and ease of processibility.<sup>[17]</sup> Some of the sources of biomass-derived hard carbon, such as chitin, bacterial cellulose, loofah, and skinned cotton, have been used as anode materials.<sup>[18–21]</sup> Coconut shells, due to their fibrous and hierarchical porous nature, have used a biomass source for the synthesis of HC and delivered a specific capacity of  $254 \text{ mAh g}^{-1}$  at a current density of  $30 \text{ mA g}^{-1}$  with 75% Coulombic efficiency.<sup>[22]</sup>

Here, hard coconut shells are used as a source for the synthesis of hard carbon (HHC) and as a reference anode material. Three types of electrolytes have been prepared such as 1 M potassium hexafluorophosphate ( $\text{KPF}_6$ ) in ethylene carbonate (EC) and di-ethylene carbonate (DEC) (1:1 v/v), 0.8 M  $\text{KPF}_6$  in EC: DEC (1:1 v/v), and 1 M potassium trifluoromethane-sulfonimide (KTFSI) in triethyleneglycol dimethyl ether

[a] R. Sahoo, R. Sundara

Alternative Energy and Nanotechnology Laboratory, Department of Physics, Indian Institute of Technology Madras, 600036 Chennai, Tamil Nadu, India  
E-mail: ramp@iitm.ac.in

[b] R. Sahoo, S. Venkatachalam

Microwave Laboratory, Department of Physics, Indian Institute of Technology Madras, 600036 Chennai, Tamil Nadu, India

(TEGDME). The effect of electrolytes on the electrochemical K ion storage of HHC was studied by discharging at a particular current density over multiple cycles. The study included qualitative analysis of the observed results by electrochemical impedance spectroscopy (EIS).

## Experimental Details

### Synthesis of Hard Coconut Shell Derived Hard Carbon (HHC)

The hard coconut shell-derived hard carbon (HHC) was synthesized by a two-step pre-carbonization and pyrolysis method.<sup>[23]</sup> The hard coconut shell was first broken into smaller parts and loaded into a quartz tube. The quartz tube was set inside a tube furnace and then heated to 500 °C at a heating rate of 5 °C/min for 5 h. After it cooled to room temperature, the pre-carbonized product was ground well to make a fine powder. The pre-carbonized carbon was carbonized at a temperature of 1100 °C for 5 h. The final product was obtained after acid-treating the carbonized powder and subsequent washing with DI water.

### Electrode and Electrolyte Preparation

The electrode was prepared using the conventional slurry coating method. A homogeneous slurry was made by grinding the active material (HHC), carbon black, and poly (vinylidene fluoride) (PVDF) in an 8:1:1 ratio and mixing well in N-methyl-2-pyrrolidone (NMP) solvent. The prepared slurry was coated on a thick copper foil using the doctor blade technique. The coated copper foil was then dried in a vacuum oven at 60 °C for 12 h, which was then calendered and cut into 12.7 mm pieces for cell fabrication.

### Fabrication of the Coin Cell and Electrochemical Measurements

The CR2032 coin cells were fabricated using the active electrode (HHC), potassium metal (Sigma Aldrich, USA, 99%) as reference/counter electrode, the desired electrolyte, and the glass fiber (GF/F, Whatmann) filter paper as the separator. All the cells were assembled inside a glove box (mBraun, UNILAB, O<sub>2</sub><0.1 ppm, H<sub>2</sub>O<0.1 ppm). The galvanostatic charge-discharge (GCD) was performed in a voltage range of 0.05–3 V, and cell stability was observed with repeated cycles using a battery tester (BCS-810, BioLogic). Electrochemical impedance spectroscopy (EIS) was utilized for the qualitative assessment of the chemical kinetics of the cell in the range of 1 kHz to 10 mHz.

## Results and Discussions

### Structural Characterization of HHC

The synthesized powder, HHC, was subjected to various structural characterizations such as X-ray diffraction (XRD), Raman spectroscopy, field emission scanning electron microscopy (FESEM), and high-resolution scanning electron microscopy (HR-TEM). The surface area and pore size of the synthesized hard carbon powder were calculated using the Brunauer–Emmett–Teller (BET) method and the Barrett–Joyner–Halenda (BJH) method, respectively.

The XRD pattern of the synthesized product exhibited two prominent peaks. Figure 1(a) displayed one broad peak centered about 24.2° and the other at 43.8° corresponding to the (002) peak and (101) peak of the amorphous carbon. The interlayer distance was calculated using Scherer's equation and was found to be around 0.36 nm, much greater than the graphite interlayer distance of 0.34 nm. The higher interlayer distance is much more beneficial for the K ion storage as, through the structure, K ions can intercalate and de-intercalate without much volume changes.<sup>[24]</sup>

Similarly, Raman spectra were obtained for the synthesized sample, as shown in Figure 1(b). Like a typical carbon material, the two prominent bands, D and G band, appeared in the spectra centered at 1340.4 cm<sup>-1</sup> and 1590.6 cm<sup>-1</sup>, respectively. The deconvoluted spectra suggested the formation of another disorder peak, D<sup>\*\*</sup>, at 1530.9 cm<sup>-1</sup>.<sup>[25]</sup> The ratio between the intensity of both D and G bands was calculated to be 1.21, suggesting the high degree of disorderness due to the pyrolysis of the biomass. Also, a broad 2D band at 2777 cm<sup>-1</sup> confirmed the presence of resonant C atoms.

The specific surface area of the synthesized hard carbon was calculated by taking BET characterization. N<sub>2</sub> gas absorption and desorption curve at 77 K suggested a type-II isotherm, as shown in Figure 1(c). The inset of the figure showed a plot between 1/Q[(P/P<sub>0</sub>)−1] vs relative pressure (P/P<sub>0</sub>), showing a linear graph. The slope and intercept of the plot were considered to calculate the relative surface area, which was found to be around 40.9 m<sup>2</sup>·g<sup>-1</sup>. Lower surface area is quite essential for the determination of Coulombic efficiency. The BJH Hass model was adopted to determine the pore size inside the structure. The BJH plot showed a distribution of nanopores (1–10 nm), micropores (10–50 nm), and macropores (50 nm and beyond), as shown in Figure 1(d).

The morphology of the synthesized powder was analyzed through FESEM and HRTEM. The pyrolyzed powder featured some systematic macro pores and long threaded flake kinds of structures, as shown in Figure 2(a). Upon magnification, some micropores were visible throughout the structure, as can be seen in Figure 2(b). The inherent nature of the coconut shell as a porous material could be the possible reason for the porous nature of the pyrolyzed powder. The highly magnified HRTEM image reaffirmed the presence of micro and nanopores on the flakes-like structure, as can be shown in Figure 2(d).

Electron dispersion spectroscopy (EDS) was carried out to identify the elements that might be present within the microscopic structure. The EDS spectra, as shown in Figure 2(c), demonstrated the presence of a high percentage of carbon (98.7%), oxygen (1.2%), and some traces of other elements such as potassium (0.1%). While high-purity carbon enhances the electron transport throughout the surface, the heterogeneous atoms present in the structure aid in the adsorption of K ion on the surface.<sup>[26]</sup>

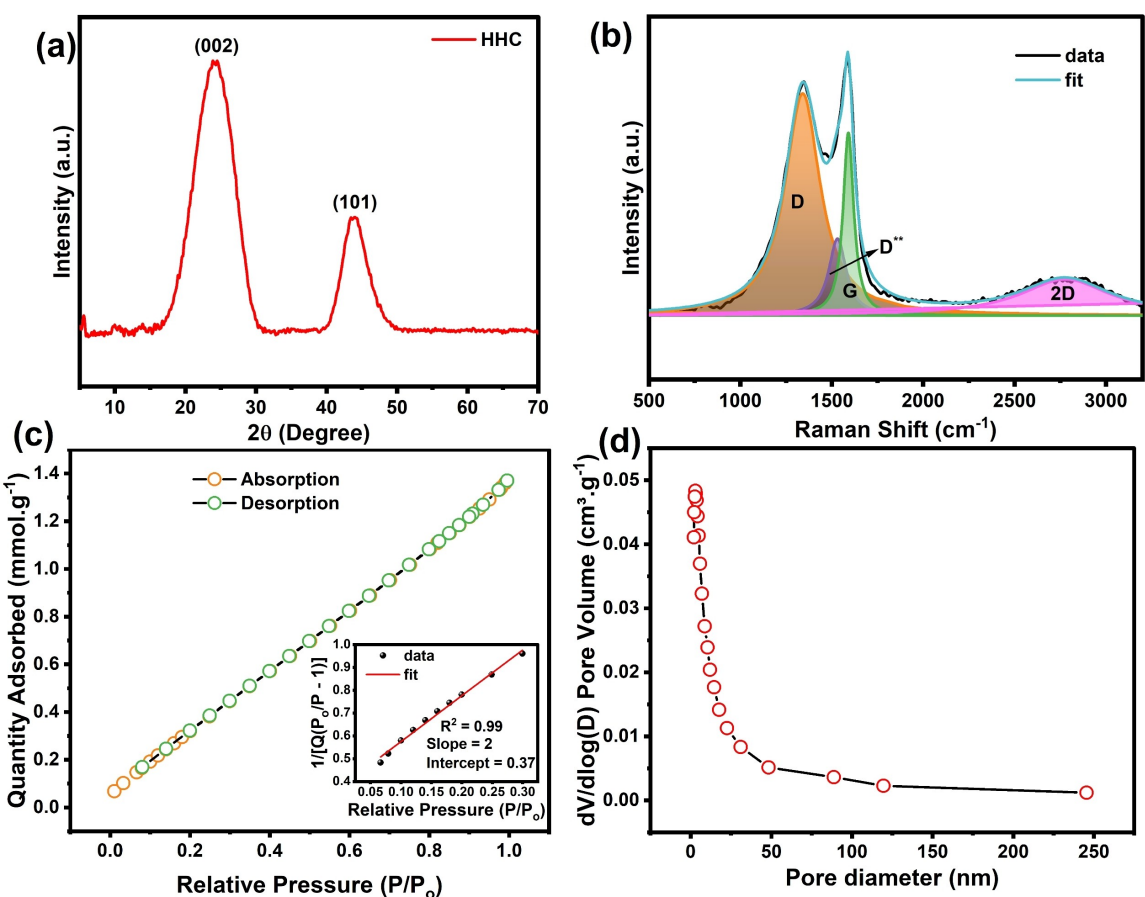


**Figure 1.** (a) XRD pattern obtained for HHC sample, (b) fitting of the Raman spectra, (c) BET surface analysis by measuring absorption and desorption curve, the inset shows a plot between  $1/Q([P/P_0] - 1)$  vs relative pressure ( $P/P_0$ ), and (d) pore distribution by BJH analysis.

### Electrochemical Performance of the Assembled Cells

The assembled cells with three different electrolytes, such as 1 M KPF<sub>6</sub> in EC: DEC (1:1 v/v), 1 M KTFSI in TEGDME, and 0.8 M KPF<sub>6</sub> in EC: DEC (1:1 v/v) were renamed to KIB-001, KIB-002, and KIB-003. The galvanostatic charge/discharge measurements were done from 0.05 V to 3 V at an initial current density of 30 mA g<sup>-1</sup> and are shown in Figure 3. KIB-001 cell showed a high initial discharge capacity of 491 mAh g<sup>-1</sup> and charge capacity of 200 mAh g<sup>-1</sup>, taking the initial Coulombic efficiency (CE) to 40.7%. The discharge capacity of the second cycle was calculated to be around 240 mAh g<sup>-1</sup>, accounting for up to 51.2% capacity loss, which could be attributed to an uneven and thick solid-liquid interphase (SEI) layer formation at the anode side. The consecutive cycles showed a better Coulombic efficiency, more than 80%, showing the reverse capability of the fabricated cell. The cell has shown a specific capacity of about 213 mAh g<sup>-1</sup> after the 10<sup>th</sup> cycle, which is about 88.75% of the 2<sup>nd</sup> cycle. However, after 20 cycles of charge and discharge, the cell degraded drastically with discharge capacity and charge capacity of 12 mAh g<sup>-1</sup> and 27 mAh g<sup>-1</sup>. Although initial cycles suggested the stability of the cell, the degradation of the cell after the 20<sup>th</sup> cycle could be attributed to inhomoge-

neous SEI layer formation at the interface and consecutive electrochemical consumption.<sup>[27]</sup>

Similarly, the KIB-002 cell, with 1 M KTFSI in TEGDME electrolyte, showed a sloping nature of charge-discharge curves, as depicted in Figure 3(b). There is a clear distinction between the initial discharge curve and the rest discharge curves. The initial discharge marked the intercalation of K ions into the anode side and the formation of the SEI layer. The SEI layer acts as a resistive layer for further de/intercalation of K ions and should be stable to enable reversibility of the cell. The initial discharge and charge capacity was determined to be around 424.3 mAh g<sup>-1</sup> and 185.1 mAh g<sup>-1</sup>, taking Coulombic efficiency (CE) to 43.6%. As expected, the second cycle discharge capacity was reduced by around 52.3% from the initial discharge capacity. However, the CE value reached about 90.4% in the second cycle and increased further up to 100% in the 20<sup>th</sup> cycle. The high CE suggests the high reversibility of the cell. Upon further cycling, the specific capacity reduced regularly, taking to 158.1 mAh g<sup>-1</sup>, 117.8 mAh g<sup>-1</sup>, and 27.3 mAh g<sup>-1</sup> in the 5<sup>th</sup>, 10<sup>th</sup>, and 20<sup>th</sup> cycle, respectively. The systematic reduction in the capacity suggests the incompatibility of the electrolyte with the electrode. With each cycle, a part of the electrolyte was consumed due to the secondary reactions leading to the unavailability of K ions.

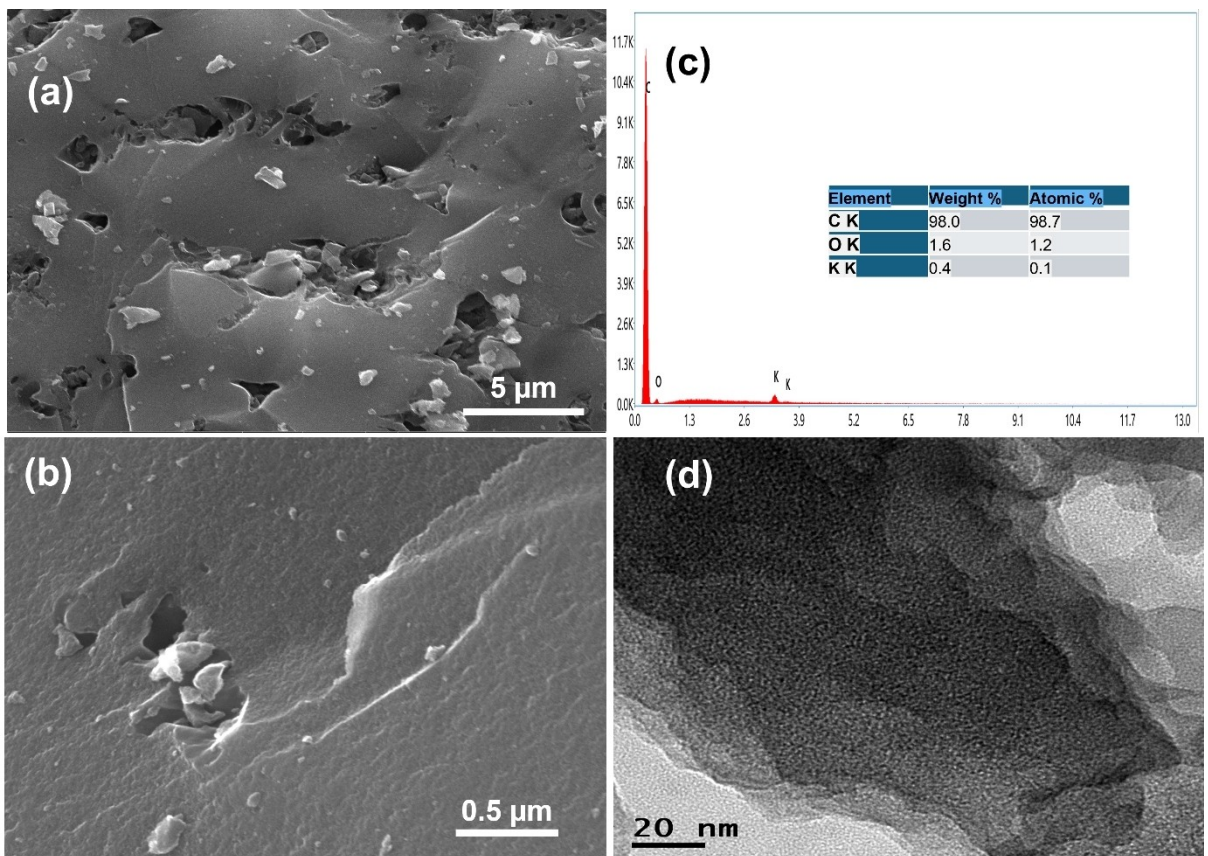


**Figure 2.** (a) FESEM image of HHC sample showing the macropores on a flake-like surface, (b) magnified image showing the uneven surface with micropores, (c) EDS of the HC confirming the presence of high purity carbon, and (d) HRTEM image of HHC sample showing distinct micro and mesopores on the surface.

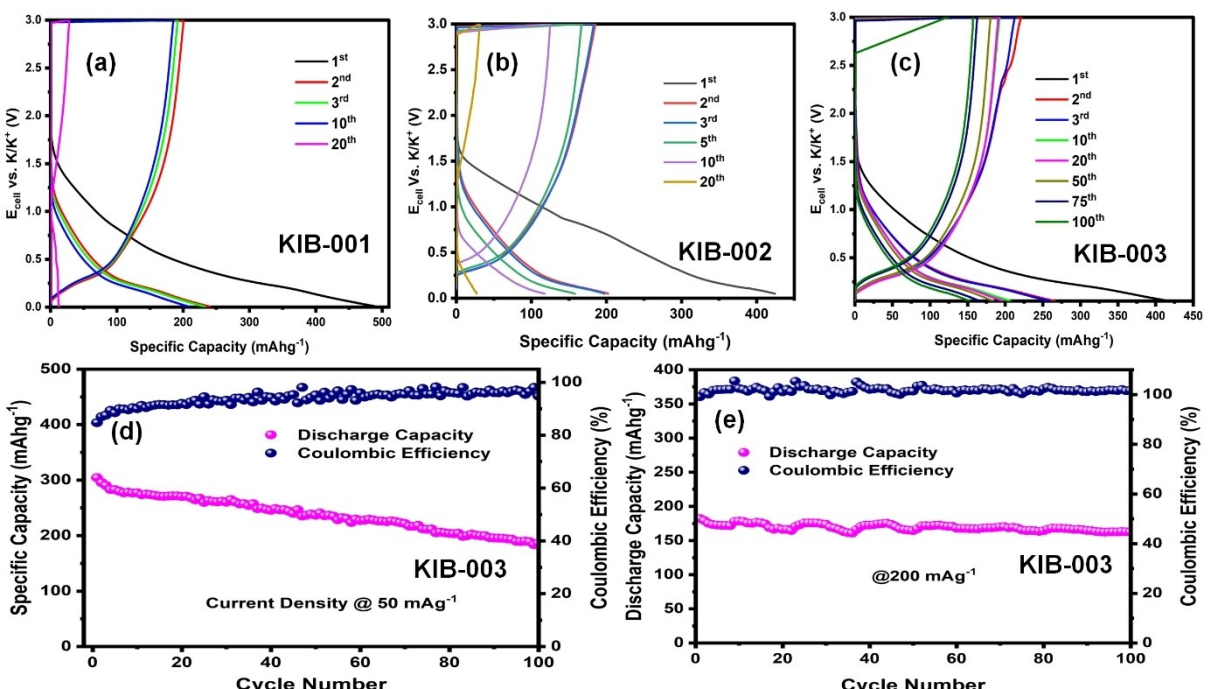


**Figure 3.** (a-c) Galvanostatic charge and discharge studies of KIB-001, KIB-002, and KIB-003 cells run at a current density of 30 mA g<sup>-1</sup>, respectively, (d-e) cyclic stability studies of KIB-003 showing discharge capacity and Coulombic efficiency at a current density of 50 mA g<sup>-1</sup> and 100 mA g<sup>-1</sup>, respectively.

The electrochemical K ion performance of KIB-003 cell assembled with 0.8 M  $\text{KPF}_6$  in EC: DEC (1:1 v/v) was shown in Figure 3(c). The initial discharge curve exhibited a constant slope-type nature and delivered a specific capacity of  $416.6 \text{ mAh g}^{-1}$  at a current density of  $30 \text{ mA g}^{-1}$ . The charging capacity was calculated to be around  $221.1 \text{ mAh g}^{-1}$ , with CE to be around 53 %. The higher CE values of KIB-003 than the other two cells suggest a better interface between the electrolyte and electrode. The consecutive discharge curves displayed a sloping nature (3–0.5 V) and a plateau nature (0.5–0.05 V). The low voltage region from 0.5–0.05 V contributed about 70 % of the total discharge capacity. The discharge capacity of the second and third cycles of the cell was nearly the same, about  $260 \text{ mAh g}^{-1}$ . As we went on cycling the cells further, the capacity decreased to  $206 \text{ mAh g}^{-1}$  after the 10<sup>th</sup> cycle (20.7 % capacity loss from the 2<sup>nd</sup> cycle). The discharge capacity decreased further steadily from the 10<sup>th</sup> to the 100<sup>th</sup> cycle with enhanced CE. The discharge capacity was determined to be around  $195.8 \text{ mAh g}^{-1}$ ,  $185 \text{ mAh g}^{-1}$ ,  $160.9 \text{ mAh g}^{-1}$ , and  $152.9 \text{ mAh g}^{-1}$  after 20<sup>th</sup>, 50<sup>th</sup>, 75<sup>th</sup>, and 100<sup>th</sup> cycles, respectively with nearly 100 % CE.

The rate capability studies of KIB-003 were carried out at a higher current rate, such as  $50 \text{ mA g}^{-1}$  and  $200 \text{ mA g}^{-1}$ , and discharged for 100 cycles to know the cyclic stability of the cell. The initial discharge capacity of the cells cycled at  $50 \text{ mA g}^{-1}$  and  $200 \text{ mA g}^{-1}$  was found to be around  $304.2 \text{ mAh g}^{-1}$  and

$187.3 \text{ mAh g}^{-1}$ , respectively, with high initial Coulombic efficiency of 84.3 % and 96.8 % as shown in Figure 3(d) and 3(e). The reduced discharge capacity suggests sluggish withdrawal/insertion of K ions into the structure. The CE of the cell applied with a current density of  $200 \text{ mA g}^{-1}$  reached 100 % in the second cycle, showing the high reversibility of the cell. The Coulombic efficiency was maintained at 100 % for the rest of the cycles. After 100 cycles, the cell run with the current density of  $50 \text{ mA g}^{-1}$  exhibited a discharge capacity of  $187.9 \text{ mAh g}^{-1}$ , retaining about 62 % of the original capacity. On the other hand, the cell run with a higher current density of  $200 \text{ mA g}^{-1}$  delivered excellent cyclic stability, retaining about 86.7 % of the original capacity with nearly 100 % efficiency.

### Electrochemical Impedance Spectroscopy Analysis

To investigate the impact of the electrolyte on the above results, we have done an EIS analysis before the cycling of the cells. EIS is an important parameter that can give us valuable information regarding the solution resistance ( $R_s$ ), charge-transfer coefficient ( $R_{ct}$ ), pseudo-capacitance ( $C_{net}$ ), and Warburg coefficient ( $W$ ). Figure 4 depicts the EIS plots with the fitted curves. The fitting model is also enclosed with the figures. All the Nyquist plots between real impedance ( $Z$ ) and imaginary impedance ( $Z'$ ) show a semi-circle at a higher frequency range

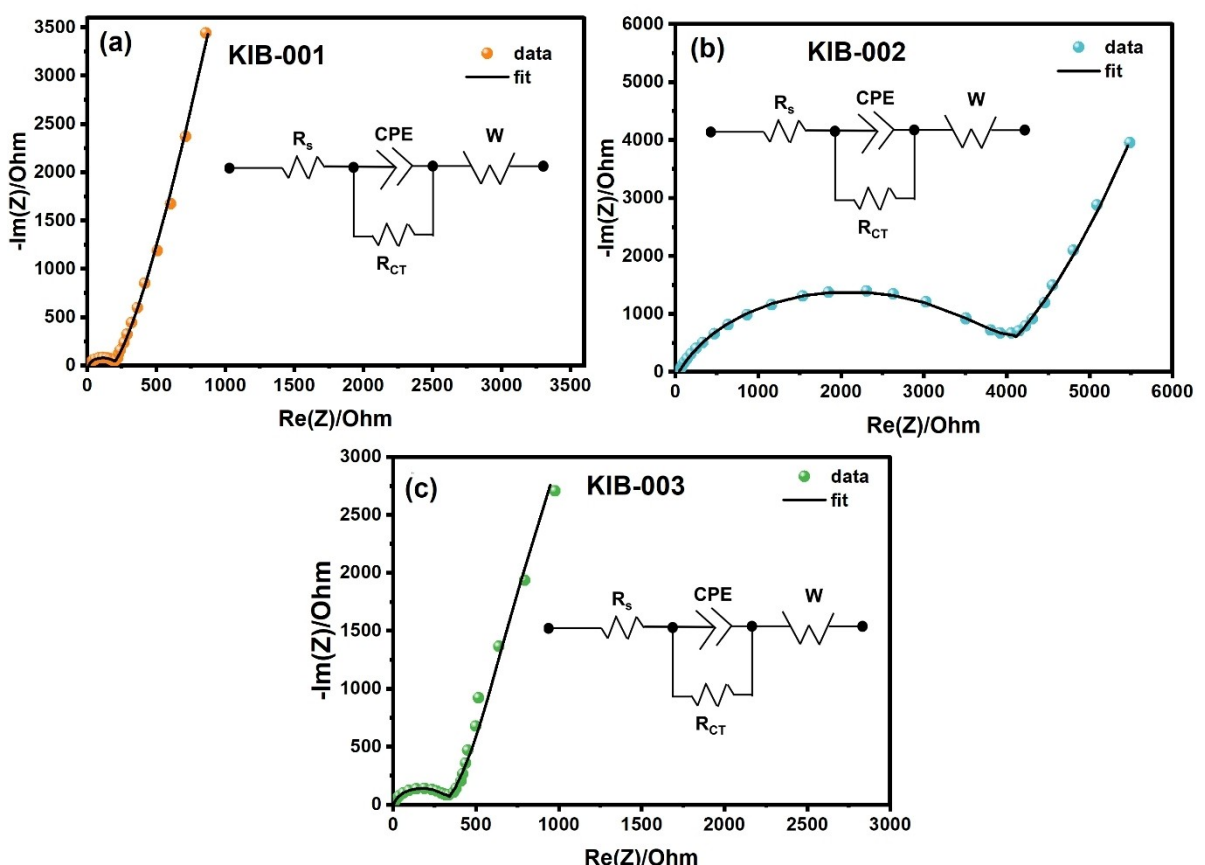


Figure 4. The observed and fitted plot between real impedance and imaginary impedance data. (a) KIB-001, (b) KIB-002, and (c) KIB-003.

(10 kHz–1 Hz) and then a linear region at a lower frequency (1 Hz–10 mHz). This can be ascribed to Randle's circuit, which suggests a mixed kinetic and diffusion-controlled behavior mechanism.<sup>[28]</sup>

The obtained data for the three cells were fitted using an equivalent circuit consisting of  $R_s$ , constant phase element (CPE),  $R_{ct}$ , and  $W$ , which is shown in the insets of Figure 4. The fitted parameters are provided in the following Table 1.

$R_s$  is an important parameter that suggests the internal resistance of the electrolyte along with other bulk materials, such as the current collector and separator. The  $R_s$  value for the KIB-001 cell is found to be 11.1 Ω, much lesser compared to 43.3 Ω of KIB-002. The least  $R_s$  value is found to be for the KIB-003 cell made with 0.8 M KPF<sub>6</sub> in EC: DEC (1:1 v/v).  $R_s$  is generally regarded as an indicator of battery aging during the cycling process.<sup>[29]</sup> Higher  $R_s$  value for the other two electrolytes suggests the further degradation of electrolytes during the cycling process. These values are reflected in the cycling process of the fabricated cells where KIB-003 outperformed the other two cells, as discussed in the previous section. The pseudo capacitance ( $C_{net}$ ) values, which are obtained from the CPE with a power coefficient, show a maximum capacitance value of 35.97 μF for KIB-003. A higher capacitance value suggests better capacity retention over cycling.

However, the charge transfer resistance ( $R_{ct}$ ) values, which tell us about the kinetics of the electrochemical reaction, show a change in pattern. The KIB-002 cell showed a maximum value of 3810 Ω followed by 292.2 Ω and 172.8 Ω of KIB-003 and KIB-001 cells, respectively. The higher the  $R_{ct}$  values, the slower the electrochemical reaction (oxidation and reduction of the chemical species).

Warburg impedance ( $W$ ) which is directly linked to the diffusion of K<sup>+</sup> in the lower frequency region. In this case, the KIB-002 cell showed the highest value of 407.9 Ω.s<sup>-1/2</sup>, followed by KIB-003 (145.7 Ω.s<sup>-1/2</sup>). The KIB-001 cell showed the lowest value of  $W$ , around 114.9 Ω.s<sup>-1/2</sup>.

To conclude, the experimental results obtained showed that the KIB-003 cell delivered better cycling retainability and rate capability than the other two cells. The EIS data revealed the least  $R_s$ , high  $C_{net}$ , and optimum values of  $R_{ct}$  and  $W$ , which paves the way for the KIB-003 cell with 0.8 M KPF<sub>6</sub> in EC: DEC (1:1 v/v) electrolyte.

### Electrolyte Exchange Experiment

For further assessment of the SEI layer formation and its impact on the electrochemical performance of the prepared HHC electrode, we performed the electrolyte exchange experiment,

which can be seen in Figure 5.<sup>[30–33]</sup> In the first case, we have assembled a new cell with 0.8 M KPF<sub>6</sub> in EC: DEC electrolyte and dis/charged for five cycles at a current density of 25 mA g<sup>-1</sup>. The initial charge capacity is calculated to be about 190 mAh g<sup>-1</sup>, and it exhibited a low Coulombic efficiency of 27.3%. In the consecutive cycles, CE enhanced to 66.6%, and the reversible capacity is 180 mAh g<sup>-1</sup>. In the fifth cycle, the reversible capacity increased further to 200 mAh g<sup>-1</sup> with a high CE of 78.7%. It can be inferred that, after the first cycle discharge capacity loss, the next consecutive cycles show consistent reversible capacity, as shown in Figure 5(a). The cell was de-assembled, and the cycled electrode was taken out to fabricate a new cell with 1 M KTFSI in TEGDME electrolyte. The initial reversible capacity was about 150 mAh g<sup>-1</sup>, which was reduced slightly to 149.1 mAh g<sup>-1</sup> for the next cycle. However, the reversible capacity reduced further to 131, 124, 115.6, and 46.4 mAh g<sup>-1</sup> for the 3<sup>rd</sup>, 5<sup>th</sup>, 10<sup>th</sup>, and 20<sup>th</sup> cycle, respectively, as shown in Figure 5(b). The re-assembled cell with 1 M KTFSI in TEGDME electrolyte regularly degraded as the number of cycles increased and retained only about 24.4% of the initial capacity, as depicted in Figure 5(c).

On the other hand, a new cell is assembled with 1 M KTFSI in TEGDME electrolyte. The cell exhibited a lower reversible capacity of 127.5 mAh g<sup>-1</sup> with a CE of 24.4% in the initial cycle. The reversible capacity further increased to 153.5 mAh g<sup>-1</sup> for the fifth cycle with an enhanced CE of 68%, as shown in Figure 5(d). However, for the comparison purpose, both reversible capacity and CE remained lower than that of the cycles performance of the cell assembled with 0.8 M KPF<sub>6</sub> in EC: DEC. After five cycles of testing, we de-assembled the cell, and the cycled HHC electrode was taken out to re-assemble with 0.8 M KPF<sub>6</sub> in EC: DEC electrolyte. The initial reversible capacity was about 228.5 mAh g<sup>-1</sup> with a high CE of 73.1%. The successive two consecutive cycles showed a slightly higher reversible capacity of 230 mAh g<sup>-1</sup>. The fifth cycle showed a reversible capacity of 251 mAh g<sup>-1</sup> with a CE of nearly 100%. However, the capacity degraded to about 228.7 mAh g<sup>-1</sup> and 188.6 mAh g<sup>-1</sup> for the 10<sup>th</sup> and 20<sup>th</sup> cycles, as can be seen in Figure 5(e). The re-assembled cell with 0.8 M KPF<sub>6</sub> in EC: DEC showed a consistent reversible capacity and retained about 82.6% of the original capacity compared to 24.4% capacity retention by the re-assembled cell with 1 M KTFSI in TEGDME. These results suggest that the formation of the SEI layer is insufficient to have stable electrochemical performance, and electrolyte properties play an important role in determining the stability of the cells.

Along with this, we have studied the EIS measurements for the cell assembled with 1 M KTFSI in TEGDME after five cycles of charge/discharge and the re-assembled with 0.8 M KPF<sub>6</sub> in EC: DEC. Figure 6 shows that after the cycling, another semi-circle has appeared along with the regular semi-circle. The extra

**Table 1.** Fitted parameters from the obtained Nyquist plots for three electrolytes.

Cell Id	Electrolyte	$R_s$ (Ω)	$C_{net}$ (μF)	$R_{ct}$ (Ω)	Warburg coefficient (Ω.s <sup>-1/2</sup> )
KIB-001	1 M KPF <sub>6</sub> in EC: DEC (1:1 v/v)	11.1	29.4	172.8	114.9
KIB-002	1 M KTFSI in TEGDME	43.3	7.9	3810	407.9
KIB-003	0.8 M KPF <sub>6</sub> in EC: DEC (1:1 v/v)	1.8	36	292.2	145.7

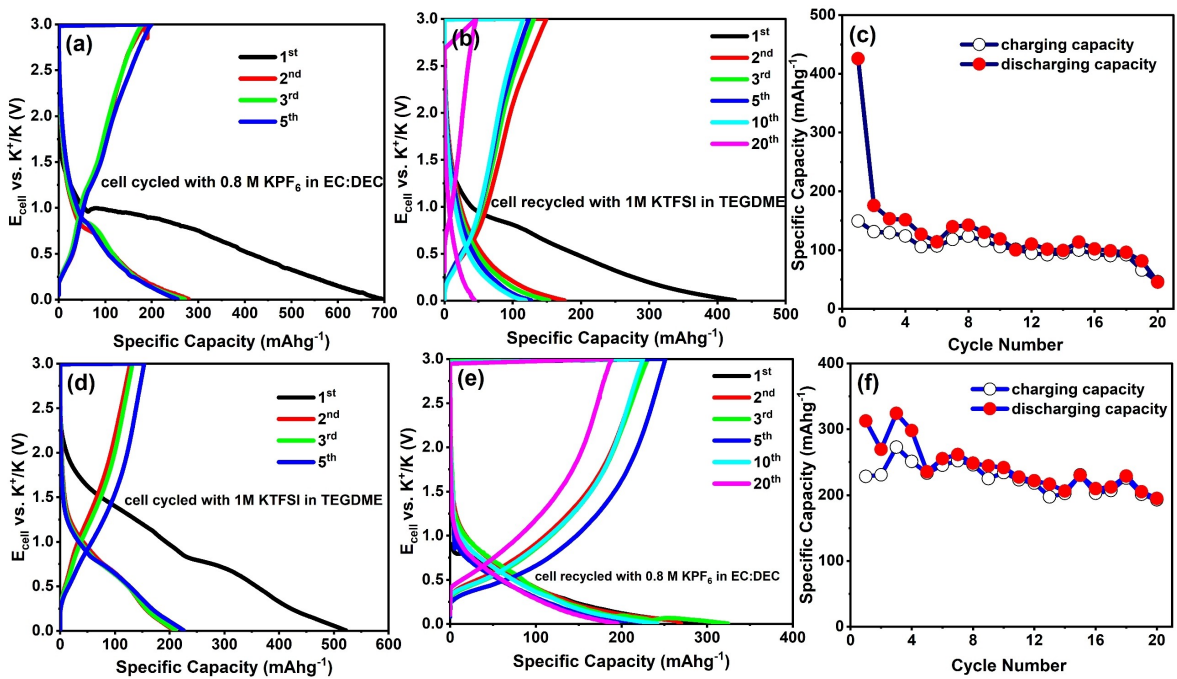


**Figure 5.** The electrolyte exchange experiment was performed to assess the stability of the SEI layer. (a) GCD profile of the cell assembled with 0.8 M KPF<sub>6</sub> in EC: DEC, (b) GCD profile of the cell at different cycles re-assembled with 1 M KTFSI in TEGDME, (c) the charge and discharge capacity recorded versus the number of cycles, (d) GCD profile of the cell assembled with 1 M KTFSI in TEGDME, (e) GCD profile of the cell at different cycle re-assembled with 0.8 M KPF<sub>6</sub> in EC: DEC, and (f) the charge and discharge capacity of the re-assembled cell recorded versus number of cycles.

**Table 2.** The comparison of electrochemical performance of the fabricated electrode with 0.8 M KPF<sub>6</sub> in EC: DEC electrolyte with previous reports.

S. No.	Biomass source	Electrolyte	Reversible capacity	Initial CE (%)	Cyclic stability	Ref
1	Coconut shell	0.8 M KPF <sub>6</sub> in EC: DEC	175.1 mAh g <sup>-1</sup> @ 100 mA g <sup>-1</sup>	94	75.9% capacity retention after 400 cycles @ 100 mA g <sup>-1</sup>	[22]
2	Coconut solid waste	5 M KFSI in DME	265.8 mAh g <sup>-1</sup> @ 25 mA g <sup>-1</sup>	–	89.2% capacity retention after 100 cycles @ 30 mA g <sup>-1</sup>	[34]
3	Coconut shell	2.5 M KFSI in triethyl phosphate	280 mAh g <sup>-1</sup> @ 50 mA g <sup>-1</sup>	87.3	92.8% capacity retention after 100 cycles @ 50 mA g <sup>-1</sup>	[35]
4	Tender coconut	0.8 M KPF <sub>6</sub> in EC: DEC	165.6 mAh g <sup>-1</sup> @ 200 mA g <sup>-1</sup>	68	98.2% capacity retention after 100 cycles @ 200 mA g <sup>-1</sup>	[23]
5	Hard coconut shell	0.8 M KPF <sub>6</sub> in EC: DEC	180.4 mAh g <sup>-1</sup> @ 200 mA g <sup>-1</sup>	96.3	86.7% capacity retention after 100 cycles @ 200 mA g <sup>-1</sup>	This work

semi-circle could be attributed to the formation of the SEI layer. However, after re-assembling the cell with 0.8 M KPF<sub>6</sub> in EC: DEC, the extra semi-circle disappeared. Moreover, the R<sub>ct</sub> reduced to 510.7 Ω from 3506 Ω after the re-assembling of the cell with 0.8 M KPF<sub>6</sub> in EC: DEC. This affirms the role of microstructural properties of electrolytes controlling the electrochemical performance of the electrode.

The electrochemical performance, reversible capacity, Coulombic efficiency, and cyclic stability of HHC with 0.8 M KPF<sub>6</sub> in EC: DEC (1:1 v/v) electrolyte was compared with previous studies for electrodes obtained from coconut shells with different electrolytes as depicted in Table 2. Compared to the previous reports, our fabricated electrode shows a higher Coulombic efficiency at a relatively higher current density.

## Conclusions

A two-step pre-carbonization and pyrolysis method was adopted to synthesize hard carbon from hard coconut shells and used as an anode material. The synthesized HC showed an interplanar spacing of 0.36 nm larger than that of graphite. FESEM and HRTEM images exhibited irregular and porous structures. The BET surface area was calculated to be 40.9 m<sup>2</sup>·g<sup>-1</sup>. For the electrochemical characterization, CR2032-type coin cells were fabricated with three types of electrolytes. The cell with 0.8 M KPF<sub>6</sub> in EC: DEC (1:1 v/v) outperformed the other two cells by retaining over 86.7% of the original capacity after 100 cycles. EIS studies verified that lower solution resistance, higher pseudo capacitance, and optimum charge

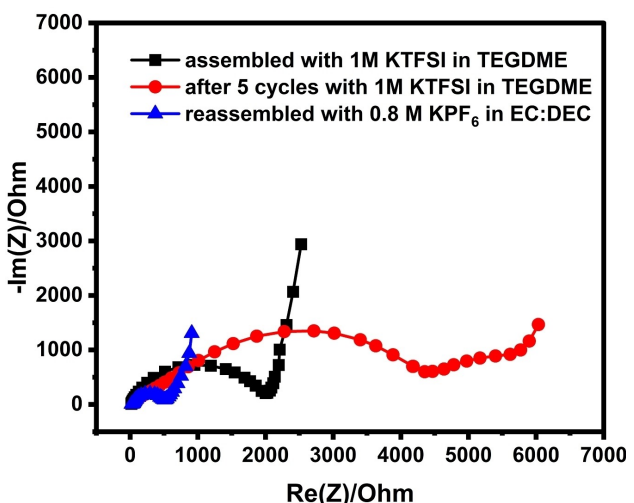


**Figure 6.** EIS studies the cell assembled with 1 M KTFI in TEGDME and reassembled with 0.8 M KPF<sub>6</sub> in EC: DEC.

transfer resistance are the reasons for the stable capacity over cycles of charge and discharge.

## Acknowledgments

The authors would like to acknowledge the Department of Physics, Indian Institute of Technology Madras, for the experimental facilities.

## Conflict of Interests

The authors declare no conflict of interest.

## Data Availability Statement

The data that support the findings of this study are available from the corresponding author upon reasonable request.

**Keywords:** Biowaste · Hard carbon · Electrolytes · Potassium ion batteries · Electrochemical impedance spectroscopy

- [1] F. Alanazi, *Appl. Sci.* **2023**, *13*, 6016.
- [2] X. Zhao, H. Hu, H. Yuan, X. Chu, *Heliyon* **2023**, *9*, e20296.
- [3] S. Chandra, "EVs and India's Net Zero goals," can be found under <https://www.financialexpress.com/opinion/evs-and-indias-net-zero-goals/3397848/>, 2024.
- [4] M. Carlier, "Batteries share of large EV costs 2016–2030," can be found under <https://www.statista.com/statistics/797638/battery-share-of-large-electric-vehicle-cost/>, 2017.

- [5] R. Rajagopalan, Y. Tang, X. Ji, C. Jia, H. Wang, *Adv. Funct. Mater.* **2020**, *30*, 1909486.
- [6] X. Wu, S. Qiu, Y. Liu, Y. Xu, Z. Jian, J. Yang, X. Ji, J. Liu, *Adv. Mater.* **2022**, *34*, 2106876.
- [7] K. Sada, J. Darga, A. Manthiram, *Adv. Energy Mater.* **2023**, *13*, DOI 10.1002/aenm.202302321.
- [8] S. Liu, L. Kang, J. Henzie, J. Zhang, J. Ha, M. A. Amin, M. S. A. Hossain, S. C. Jun, Y. Yamauchi, *ACS Nano* **2021**, *15*, 18931–18973.
- [9] M. Zhou, P. Bai, X. Ji, J. Yang, C. Wang, Y. Xu, *Adv. Mater.* **2021**, *33*, 1–22.
- [10] H. Xie, H. Liang, P. Kumar, H. Cheng, F. Zhao, Y. Wang, T. Cai, W. Wahyudi, Z. Ma, Q. Li, J. Ming, *Adv. Funct. Mater.* **2024**, *34*, DOI 10.1002/adfm.202401118.
- [11] G. Liu, Z. Cao, L. Zhou, J. Zhang, Q. Sun, J. Hwang, L. Cavallo, L. Wang, Y. Sun, J. Ming, *Adv. Funct. Mater.* **2020**, *30*, DOI 10.1002/adfm.202001934.
- [12] W. Liu, T. Shi, F. Liu, C. Yang, F. Qiao, K. Han, C. Han, J. Meng, X. Wang, *Nanomaterials* **2024**, *14*, 550.
- [13] S. Trano, D. Versaci, M. Castellino, M. Fontana, L. Fagioli, C. Francia, F. Bella, *Energy Mater.* **2024**, *4*, DOI 10.20517/energymater.2023.79.
- [14] Z. Jian, W. Luo, X. Ji, *J. Am. Chem. Soc.* **2015**, *137*, 11566–11569.
- [15] L. Zhong, W. Zhang, S. Sun, L. Zhao, W. Jian, X. He, Z. Xing, Z. Shi, Y. Chen, H. N. Alshareef, X. Qiu, *Adv. Funct. Mater.* **2023**, *33*, DOI 10.1002/adfm.202211872.
- [16] H. Lei, J. Li, X. Zhang, L. Ma, Z. Ji, Z. Wang, L. Pan, S. Tan, W. Mai, *InfoMat* **2022**, *4*, DOI 10.1002/inf2.12272.
- [17] X. Yuan, B. Zhu, J. Feng, C. Wang, X. Cai, R. Qin, *Chem. Eng. J.* **2021**, *405*, 126897.
- [18] C. Chen, Z. Wang, B. Zhang, L. Miao, J. Cai, L. Peng, Y. Huang, J. Jiang, Y. Huang, L. Zhang, J. Xie, *Energy Storage Mater.* **2017**, *8*, 161–168.
- [19] H. Li, Z. Cheng, Q. Zhang, A. Natan, Y. Yang, D. Cao, H. Zhu, *Nano Lett.* **2018**, *18*, 7407–7413.
- [20] Z. Wu, L. Wang, J. Huang, J. Zou, S. Chen, H. Cheng, C. Jiang, P. Gao, X. Niu, *Electrochim. Acta* **2019**, *306*, 446–453.
- [21] X. He, J. Liao, Z. Tang, L. Xiao, X. Ding, Q. Hu, Z. Wen, C. Chen, *J. Power Sources* **2018**, *396*, 533–541.
- [22] T. Huang, D. Peng, Z. Chen, X. Xia, Y. Chen, H. Liu, *New. Carbon. Mater.* **2022**, *37*, 1125–1132.
- [23] R. Sahoo, B. Tharigopala Vincent, L. Thirugnamam, S. Venkatachalam, R. Sundara, *ACS Appl. Energ. Mater.* **2024**, *7*, 7006–7018.
- [24] L. Tao, L. Liu, R. Chang, H. He, P. Zhao, J. Liu, *J. Power Sources* **2020**, *463*, 228172.
- [25] A. Kaniyoor, S. Ramaprabhu, *AIP Adv.* **2012**, *2*, DOI 10.1063/1.4756995.
- [26] Y. Wang, F. Yuan, Z. Li, D. Zhang, Q. Yu, B. Wang, *APL Mater.* **2022**, *10*, DOI 10.1063/5.0086874.
- [27] X. Wang, H. Wang, *Adv. Powder Mater.* **2022**, *1*, 100057.
- [28] W. Choi, H.-C. Shin, J. M. Kim, J.-Y. Choi, W.-S. Yoon, *J. Electrochem. Sci. Technol.* **2020**, *11*, 1–13.
- [29] S. Barcellona, S. Colnago, G. Dotelli, S. Latorrata, L. Piegari, *J. Energy Storage* **2022**, *50*, 104658.
- [30] Q. Li, G. Liu, P. Kumar, F. Zhao, Y. Wang, T. Cai, Y. Chen, H. Xie, W. Wahyudi, Z. Ma, J. Ming, *Adv. Funct. Mater.* **2024**, *2416714*, DOI 10.1002/adfm.202416714.
- [31] J. Wang, P. Kumar, Z. Ma, H. Liang, F. Zhao, H. Xie, Y. Wang, T. Cai, Z. Cao, L. Cavallo, Q. Li, J. Ming, *ACS Energy Lett.* **2024**, *9*, 4386–4398.
- [32] J. Zhang, Z. Cao, L. Zhou, G. Liu, G.-T. Park, L. Cavallo, L. Wang, H. N. Alshareef, Y.-K. Sun, J. Ming, *ACS Energy Lett.* **2020**, *5*, 2651–2661.
- [33] J. Ming, Z. Cao, Y. Wu, W. Wahyudi, W. Wang, X. Guo, L. Cavallo, J.-Y. Hwang, A. Shamim, L.-J. Li, Y.-K. Sun, H. N. Alshareef, *ACS Energy Lett.* **2019**, *4*, 2613–2622.
- [34] Y. Ma, W. Liu, W. Liu, G. Zhang, Y. Wang, H. Wang, W. Chen, M. Huang, X. Wang, *Coating* **2024**, *14*, 208.
- [35] L. Tan, J. Chen, L. Wang, N. Li, Y. Yang, Y. Chen, L. Guo, X. Ji, Y. Zhu, *Batteries & Supercaps* **2024**, *7*, DOI 10.1002/batt.202400010.

Manuscript received: October 21, 2024  
Revised manuscript received: December 2, 2024  
Accepted manuscript online: January 7, 2025  
Version of record online: January 10, 2025